Springer

KSME

Journal of Mechanical Science and Technology 33 (11) (2019) 5251~5260
www.springerlink.com/content/1738-494x(Print)/1976-3824(Online)
DOI 10.1007/s12206-019-1016-4

Numerical study on the dynamic behavior of multiple rising bubbles using the lattice Boltzmann method †

Namgyun Jeong*

Mechanical Engineering, Inha Technical College, Incheon 22212, Korea

(Manuscript Received December 28, 2018; Revised July 24, 2019; Accepted August 12, 2019)

Abstract

For numerical analysis of multiphase flow, each interface boundary should be captured, and the geometric deformation of the interface needs to be predicted. To predict the interface, the singular interface model and diffusion interface model can be used. Among them, free energy based lattice Boltzmann method has adopted the diffusion interface model, with which it is easy to simulate complex multiphase flow phenomena such as bubble collapse, droplet collision, and moving contact lines. A new lattice Boltzmann method for the simulation of multiphase flows is described, and test results for the validation are presented. Finally, some simulations were carried out for the investigation of dynamic behavior of multiple rising bubbles.

Keywords: Mutiphase flow; Rising bubble; Lattice Boltzmann method; Free energy

1. Introduction

In multiphase flow, which includes at least two phases among gas, liquid, and solid, the phenomena get to be shown differently with the flow having a single phase because the fluids with different property flows mutually interact with each other. Various investigations [1-4] have been carried out with experimental and numerical ways to declare or estimate these phenomena exactly because they are very important for not only academic studies but also industrial applications.

For the simulation of multiphase flow, conventional CFD solving the Navier- Stokes equation has been mainly carried out with several interface capturing method such as the volume of fluid method [5], level set method [6], and front-tracking technique [7]. However, these traditional approaches do not easily capture the interface boundary in dealing with complex multiphase flow phenomenon such as bubble collapse, droplet collision etc.

Recently, the lattice Boltzmann method (LBM) has appeared as an alternative tool. The first LBM model for the simulation of multiphase flow is color gradient model proposed by Gunstensen et al. [8] and modified by Grunau et al. [9]. In their models, red and blue colored particles are introduced to represent two different fluids. The sustenance of interface and the separation of phases are achieved by the repulsive interaction based on the color gradient and color momentum. Shan and Chen [10] used interaction potential between particles at neighboring lattice sites to control the form of the equation of state (EOS) of the fluid, called pseudo-potential model. Swift et al. [11] proposed a free energy based model. In their model, a non-ideal pressure tensor, which is derived from the free-energy function of non-uniform fluids, and an external chemical potential are introduced to obtain an isothermal model of phase separation. He et al. [12] presented a multiphase LBM in the nearly incompressible limit. In their model, the interfacial dynamics is modeled by incorporating molecular interactions, and two particle distribution functions are used to simulate pressure and velocity fields and to track the density field.

Although the density ratio of the different fluids can vary with large range in practical problems, the above-mentioned methods are restricted to low density ratios. Therefore, some researchers have attempted to suggest an improved LBM for higher density ratios up to 1000. Among them, Zheng et al. [13] and Lee and Liu [14] are representative. Their models are based on a free energy approach, and they use two sets of particle distributions for the hydrodynamics of the flow and for the interface capturing. In the model of Zheng et al. [13], the Cahn-Hilliard equation (CHE) to capture the interface is completely recovered without any additional term unlike that of Lee and Liu [14], and their method can be easily implemented. However, this method is unable to simulate two phase flow that needs to use densities of fluids separately for each phase, because the model uses mean value of two densities in the whole computational domain. On the other hand, the

*Corresponding author. Tel.: +82 328702132, Fax.: +82 328702500
E-mail address: nkjung@inhatc.ac.kr
† Recommended by Associate Editor Hyoung Gwon Choi

model of Lee and Liu [14] uses real density of the fluid, so that the density ratio effect on the flow can be examined. However, the equation in the model of Lee and Liu [14] is more complicated, and it needs much more calculation time than the model in Ref. [13]. In addition, a second derivative of chemical potential has to be used in the CHE.

The objective of this paper is to suggest a new LBM approach which compensates for the short comings of the models in Refs. [13, 14]. For the pressure evolution equation, the same model that Lee and Liu [14] suggested is used to impose the real density for each phase, and a simple lattice Boltzmann equation with the equilibrium distribution function given by Ref. [15] is adopted for the CHE to reduce the complexity and calculation time when capturing the interface. The rest of this paper is organized as follows. In Sec. 2, the multiphase LBM of this study is described. Numerical simulations for validation are carried out in Sec. 3. In Sec. 4, the results of multiple bubble rising under the gravitational force are shown.

2. Multiphase lattice Boltzmann method

2.1 Pressure evolution and momentum transport equation

When two different phases, whose densities are ρ_l and ρ_g ($\rho_l > \rho_g$), are mixed, the discrete Boltzmann equation for the pressure evolution and momentum transport equation can be given as follows [14]:

$$\frac{\partial f_\alpha}{\partial t} + \vec{e}_\alpha \cdot \nabla f_\alpha = -\frac{1}{\lambda}\left(f_\alpha - f_\alpha^{eq}\right) + \left(\vec{e}_\alpha - \vec{u}\right)\cdot\left[\nabla \rho c_s^2\left(\Gamma_\alpha - \Gamma_\alpha(0)\right) - \varphi \nabla \mu_\varphi \Gamma_\alpha\right] \tag{1}$$

$$f_\alpha^{eq} = w_\alpha\left[p + \rho c_s^2\left(\frac{\vec{e}_\alpha\cdot\vec{u}}{c_s^2} + \frac{\left(\vec{e}_\alpha\cdot\vec{u}\right)^2}{2c_s^4} - \frac{\left(\vec{u}\cdot\vec{u}\right)}{2c_s^2}\right)\right] \tag{2}$$

$$\Gamma_\alpha = \Gamma_\alpha\left(\vec{u}\right) = w_\alpha\left[1 + \frac{\vec{e}_\alpha\cdot\vec{u}}{c_s^2} + \frac{\left(\vec{e}_\alpha\cdot\vec{u}\right)^2}{2c_s^4} - \frac{\left(\vec{u}\cdot\vec{u}\right)}{2c_s^2}\right] \tag{3}$$

where f_α is the particle distribution function, $\vec{e}_\alpha$ is the α-direction microscopic particle velocity, p is the pressure, φ is the order parameter, μ_φ is the chemical potential, w_α is the weighting factor, c_s is the sound speed, and λ is the relaxation time. For the lattice model, the square lattice (D2Q9) is used. The set of discrete velocities is

$$\vec{e}_\alpha = \begin{cases} 0 & \alpha = 0 \\ \cos\left(\frac{(\alpha-1)\pi}{4}\right)\vec{i} + \sin\left(\frac{(\alpha-1)\pi}{4}\right)\vec{j} & \alpha = 1,3,5,7 \\ \sqrt{2}\left\{\cos\left(\frac{(\alpha-1)\pi}{4}\right)\vec{i} + \sin\left(\frac{(\alpha-1)\pi}{4}\right)\vec{j}\right\} & \alpha = 2,4,6,8 \end{cases} \tag{4}$$

and the weighting factor w_α is

$$w_\alpha = \begin{cases} 4/9 & \alpha = 0 \\ 1/9 & \alpha = 1,3,5,7 \\ 1/36 & \alpha = 2,4,6,8 \end{cases} \tag{5}$$

By discretizing Eq. (1) along with the characteristic over the time step δt using the modified particle distribution function $\overline{f_\alpha}$, following equation can be obtained [14]:

$$\overline{f_\alpha}\left(\vec{x} + \vec{e}_\alpha\delta t, t + \delta t\right) = \overline{f_\alpha}\left(\vec{x}, t\right) - \frac{1}{\tau_f + \frac{1}{2}}\left(\overline{f_\alpha} - \overline{f_\alpha}^{eq}\right)\Big|_{(\vec{x},t)} + \delta t\left(\vec{e}_\alpha - \vec{u}\right)\cdot\left[\nabla\rho c_s^2\left(\Gamma_\alpha - \Gamma_\alpha(0)\right) - \varphi\nabla\mu_\varphi\Gamma_\alpha\right]\Big|_{(\vec{x},t)}, \tag{6}$$

$$\overline{f_\alpha} = f_\alpha + \frac{1}{2\tau_f}\left(f_\alpha - f_\alpha^{eq}\right) - \frac{\delta t}{2}\left(\vec{e}_\alpha - \vec{u}\right)\cdot\left[\nabla\rho c_s^2\left(\Gamma_\alpha - \Gamma_\alpha(0)\right) - \varphi\nabla\mu_\varphi\Gamma_\alpha\right], \tag{7}$$

$$\overline{f}_\alpha^{eq} = f_\alpha^{eq} - \frac{\delta t}{2}\left(\vec{e}_\alpha - \vec{u}\right)\cdot\left[\nabla\rho c_s^2\left(\Gamma_\alpha - \Gamma_\alpha(0)\right) - \varphi\nabla\mu_\varphi\Gamma_\alpha\right], \tag{8}$$

where $\tau_f\left(=\lambda/\delta t\right)$ is the non-dimensional relaxation time which is related to the kinematic viscosity ν as $\nu = \tau_f c_s^2\,\delta t$. The momentum and pressure can be obtained by calculation of the zeroth and first moments of $\overline{f_\alpha}$:

$$\rho\vec{u} = \frac{1}{c_s^2}\sum_\alpha \vec{e}_\alpha\overline{f_\alpha} - \frac{\delta t}{2}\varphi\nabla\mu_\varphi, \tag{9}$$

$$p = \sum_\alpha \overline{f_\alpha} + \frac{\delta t}{2}\vec{u}\cdot\nabla\rho c_s^2. \tag{10}$$

2.2 Interface capturing equation

The interface capturing equation is modeled by Cahn-Hilliard equation:

$$\frac{\partial\varphi}{\partial t} + \nabla\cdot\left(\varphi\vec{u}\right) = \theta_M\nabla^2\mu_\varphi, \tag{11}$$

where θ_M is the mobility. After getting the order parameter φ, the density can be taken as $\rho = \varphi\rho_l + (1-\varphi)\rho_g$. The chemical potential μ_φ can be derived from the free energy density functional as $\mu_\varphi = 4\beta\varphi(\varphi-1)(\varphi-0.5) - \kappa\nabla^2\varphi$. The profile of φ along the normal direction of the interface at equilibrium is $\varphi(z) = 1/2 + 1/2\tanh(2z/W)$, where z is the coordinate normal to the interface, and W is the interface thickness. Given W and β, the gradient parameter κ and surface tension coefficient σ can be obtained as $\kappa = \beta W^2/8$, $\sigma = \sqrt{2\kappa\beta}/6$.

To derive the Cahn-Hilliard equation, Lee and Liu [14] used the following equation:

$$\overline{g}_\alpha\left(\vec{x} + \vec{e}_\alpha\delta t, t + \delta t\right) = \overline{g}_\alpha\left(\vec{x}, t\right) - \frac{1}{\tau_\varphi + \frac{1}{2}}\left(\overline{g}_\alpha - \overline{g}_\alpha^{eq}\right)\Big|_{(\vec{x},t)}, \tag{12}$$

$$+\delta t\left(\vec{e}_\alpha-\vec{u}\right)\cdot\left[\nabla\varphi-\frac{\varphi}{\rho c_s^2}\left(\nabla p+\varphi\nabla\mu_\varphi\right)\right]\Gamma_\alpha\Big|_{(\vec{x},t)}$$

$$+\frac{\delta t}{2}\theta_M\nabla^2\mu_\varphi\Gamma_\alpha\Big|_{(\vec{x},t)}+\frac{\delta t}{2}\theta_M\nabla^2\mu_\varphi\Gamma_\alpha\Big|_{(\vec{x}+\vec{e}_\alpha\delta t,t+\delta t)}$$

$$\bar{g}_\alpha^{eq}=g_\alpha^{eq}-\frac{\delta t}{2}\left(\vec{e}_\alpha-\vec{u}\right)\cdot\left[\nabla\varphi-\frac{\varphi}{\rho c_s^2}\left(\nabla p+\varphi\nabla\mu_\varphi\right)\right]\Gamma_\alpha, \quad (13)$$

$$g_\alpha^{eq}=w_\alpha\varphi\left[1+\frac{\vec{e}_\alpha\cdot\vec{u}}{c_s^2}+\frac{\left(\vec{e}_\alpha\cdot\vec{u}\right)^2}{2c_s^4}-\frac{\left(\vec{u}\cdot\vec{u}\right)}{2c_s^2}\right]. \quad (14)$$

When Eqs. (6) and (12) are compared with the LB equations of Zheng et al. [13], they are more complicated and need higher calculation time. In addition, the second-order derivative of μ_φ needs to be calculated, and $\delta t/2\theta_M\nabla^2\mu_\varphi\Gamma_\alpha\big|_{(\vec{x}+\vec{e}_\alpha\delta t,t+\delta t)}$ should be approximated by $\delta t/2\theta_M\nabla^2\mu_\varphi\Gamma_\alpha\big|_{(\vec{x}+\vec{e}_\alpha\delta t,t)}$.

The complexity of the above LB equations are due to the fact that they related the particle distribution function g_α for the composition φ to h_α by $g_\alpha=(\varphi/\rho)h_\alpha$ and $g_\alpha^{eq}=(\varphi/\rho)h_\alpha^{eq}$, where h_α is the particle distribution function for the discrete Boltzmann equation for the transport of the mixture density and momentum of incompressible binary fluids given as

$$\frac{\partial h_\alpha}{\partial t}+\vec{e}_\alpha\cdot\nabla h_\alpha=-\frac{1}{\lambda}\left(h_\alpha-h_\alpha^{eq}\right)+\frac{1}{c_s^2}\left(\vec{e}_\alpha-\vec{u}\right)\cdot\vec{F}\Gamma_\alpha. \quad (15)$$

$\vec{F}(=\nabla\rho c_s^2-\nabla p+\varphi\nabla\mu_\varphi)$ is the intermolecular force. Eq. (15) can be transformed into Eq. (1) with the assumption of low Mach number.

However, the particle distribution function for the interface capturing does not have to be related to that for the density and momentum as shown in Ref. [13]. In this study, a simple LB equation is used to overcome the short comings of Eq. (12):

$$g_\alpha\left(\vec{x}+\vec{e}_\alpha\delta t,t+\delta t\right)=g_\alpha\left(\vec{x},t\right)-\frac{1}{\tau_\varphi+\frac{1}{2}}\left(g_\alpha-g_\alpha^{eq}\right)\Big|_{(\vec{x},t)}. \quad (16)$$

The chemical potential μ_φ is included in the equilibrium distribution function as follows [15]:

$$g_\alpha^{eq}=w_\alpha\left[B_\alpha+\varphi\frac{\vec{e}_\alpha\cdot\vec{u}}{c_s^2}\right]. \quad (17)$$

$$B_\alpha=\begin{cases}\dfrac{\gamma\mu_\varphi}{c_s^2}=B & (\alpha>0)\\ w_\alpha^{-1}\left[\varphi-\left(1-w_\alpha\right)B\right] & (\alpha=0)\end{cases} \quad (18)$$

Here γ is related to θ_M as $\theta_M=\tau_\varphi\gamma\delta t$, and the order parameter φ can be obtained as $\varphi=\sum_\alpha g_\alpha=\sum_\alpha g_\alpha^{eq}$. The Cahn-Hilliard equation presented in Eq. (11) can be obtained when Chapman-Enskog multiscale analysis [16] is applied to this model in the long-time and long-wavelength limit.

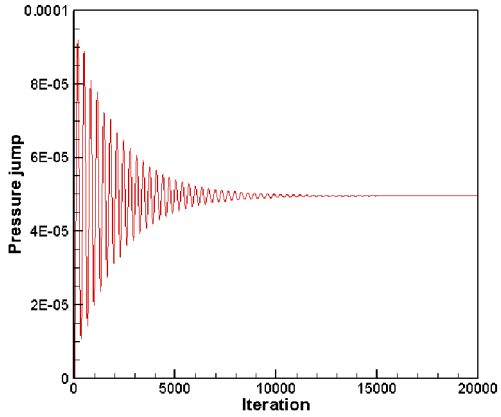

Fig. 1. Variation of the pressure jump over time.

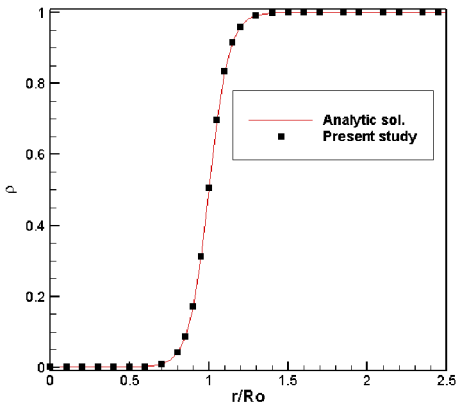

Fig. 2. Variation in density along the radial direction from the bubble center.

3. Validation

3.1 A bubble in the stationary flow

A benchmark test was carried out for the circular bubble placed at the center of the stationary liquid. In the computational domain 100 x 100 lattice cells are used, and the periodic condition is employed at all boundaries. The parameters are set as $\rho_l=1$, $\rho_g=0.001$, $\tau_f=0.3$, $\tau_\varphi=0.5$, $\sigma=0.001$, $\gamma=0.01$, and $W=5$. The diameter of bubble is 40 in lattice unit. If the pressure is properly calculated in the bubble and surrounding liquid, then the bubble shape will remain the same even after a long time, and the pressure jump(Δp) across the phase interface will also be satisfied with the Laplace law $\Delta p=\sigma/R$, where R is the radius of the bubble.

Fig. 1 shows the variation of the pressure jump over time. It is seen that the value is oscillating early in the calculation, and the amplitude decreases until 15000 time steps. Fig. 2 shows the variation in density along the radial direction from the bubble center after 50000 time steps. The distance is normal-

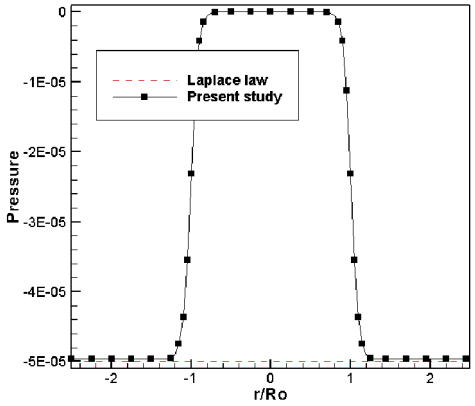

Fig. 3. Distribution of pressure around the bubble.

ized by the initial radius of the bubble. The result agrees well with the analytic solution.

In Fig. 3, the distribution of pressure around the bubble is shown. The pressure is expressed as the relative value to the pressure at the center of the bubble. Then, the pressure at the outside of the bubble should be 5×10^{-5} by the Laplace law. The pressure is nearly identical with the analytic solution showing an error of approximately 0.7 %.

3.2 Rayleigh Taylor instability

The next test for the validation is the problem of the Rayleigh-Taylor instability, which occurs when a heavier fluid lies on a lighter fluid in a gravitational field. If there is an interface perturbation, the heavy liquid moves down forming a spike and the light liquid travels up. Two important parameters in studying on Rayleigh-Taylor instability are the Atwood number $At=(\rho_l-\rho_g)/(\rho_l+\rho_g)$, and the Reynolds number $Re=d\sqrt{gd}/\nu$, where d is the characteristic length and g is the gravitational acceleration.

The simulation was carried out in a two-dimensional domain of [-64,64] x [-256,256]. The initial interface is disturbed as $y(x)=0.1d\cos(2\pi x/\lambda)$, where λ is the wavelength. The results for $At=0.5$, $\mathrm{Re}=256$, $\sqrt{gd}=0.04$, and $\lambda=d=128$ are compared with those of previous study [12]. Fig. 4 shows the evolution of the fluid interface at $t^*=1,2,3,4,5$, where t^* is non-dimensional time step normalized by $\sqrt{d/g}$. The patterns of the interface contour are in good agreement with those of Ref. [12]. At the early stage, the growing of the perturbation is symmetrical up and down. As time goes on, however, the heavy fluid falls into the light fluid as a spike and the light fluid rises up penetrating the heavy fluid. Then, the heavy fluid begins to roll up and forms two side spikes, which would be broken up into small droplets at a later time.

In Fig. 5, the positions of bubble front and spike tip along the time are presented. The results of this study excellently agree with the previous work.

By its definition, the Atwood number becomes larger as the density ratio increases. To verify that the model suggested in

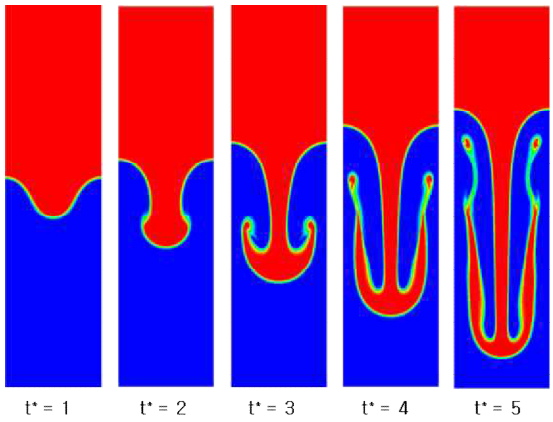

Fig. 4. The evolution of the fluid interface at t* = 0, 1, 2, 3, 4, 5 for *At* = 0.5.

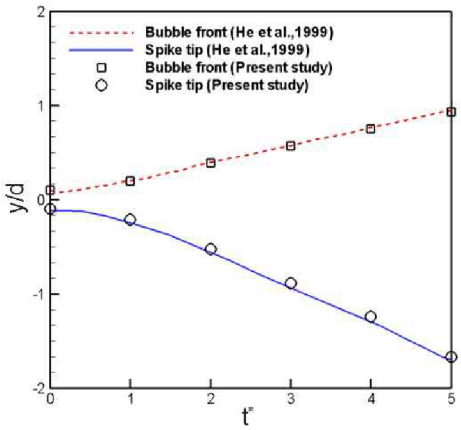

Fig. 5. Positions of bubble front and spike tip along the time for $At=0.5$.

this paper can be applied for the multiphase flow with the high density ratio, a simulation with the much higher Atwood number was conducted in a domain of [-128,128] x [-256,256]. The results for $At=0.998$, which represents the density ratio of 1000, $\mathrm{Re}=55$, and $\sqrt{gd}=0.007155$ are compared with those of ANSYS FLUENT using VOF method. In the simulations, the Weber number, $We(=\rho_l gd^2/\sigma)$, is set to 131.

Fig. 6 shows the evolution of the fluid interface at $t^*=0.5,1.0,1.5,2.0,2.5$. For large Atwood number, the heavy fluid falls in much simpler shape than that of low Atwood number, and it is hard to find the secondary instability in the later stage. The patterns of the interface contour for both methods are in good agreement. For a quantitative comparison, the positions of bubble front and spike tip along the time are shown in Fig. 7. The results of this study almost exactly agree with those of VOF method.

3.3 Single rising bubble

Bhaga and Weber [3] studied the final shape and the terminal velocity of a rising bubble by experimental way, and classified the bubble shape as spherical (S), oblate ellipsoid (OE),

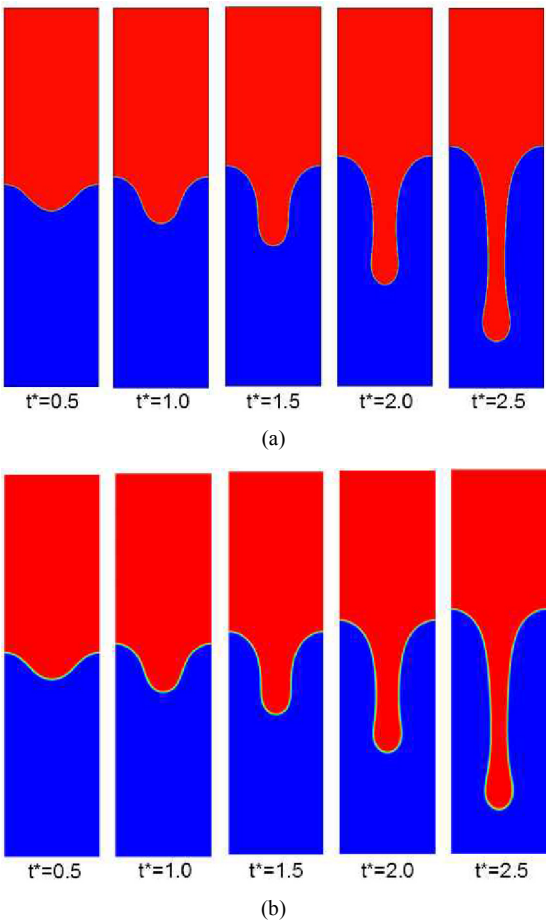

Fig. 6. The evolution of the fluid interface at t* = 0.5, 1.0, 1.5, 2.0, 2.5 for At = 0.998: (a) VOF method; (b) present study.

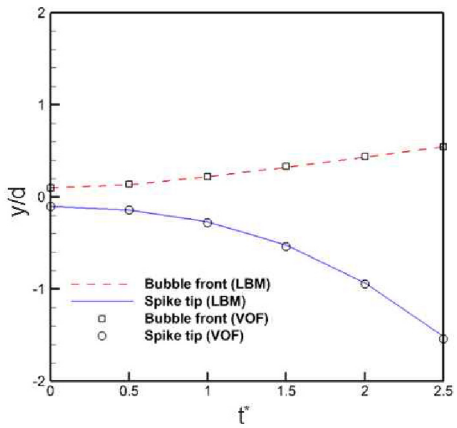

Fig. 7. Positions of bubble front and spike tip along the time for At = 0.998.

oblate ellipsoidal (OED), oblate ellipsoidal cap (OEC), spherical cap with closed, steady wake (SCC), spherical cap with open, unsteady wake (SCO), skirted with smooth, steady skirt (SKS), and skirted with wavy, unsteady skirt (SKW). These bubble types can be determined by the dimensionless parameters of Eotvos number (Eo), Morton number (M), and Reynolds number (Re):

Table 1. Comparison of numerical results for Re.

Case	Eo	M	Ryu & Ko [17]		Present study
			VOF	LBM	
A	5	0.012	5.8	6.2	5.7
B	16	0.038	9.3	12.2	9.4
C	40	0.096	14.0	16.0	15.8

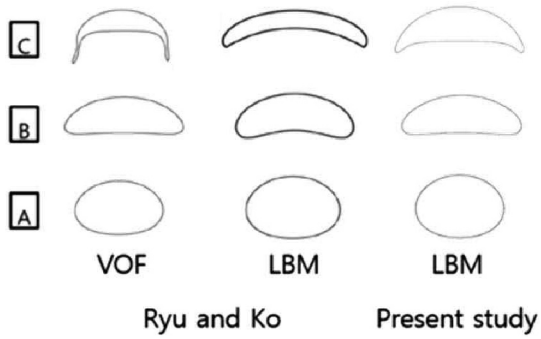

Fig. 8. Comparison of final shapes of single rising bubble.

$$Eo = \frac{g\left(\rho_l - \rho_g\right)D^2}{\sigma}, \tag{19}$$

$$M = \frac{g\left(\rho_l - \rho_g\right)\mu_l^4}{\rho_l^2\sigma^3}, \tag{20}$$

$$Re = \frac{\rho_l V_t D}{\mu_l}, \tag{21}$$

where V_t is the terminal velocity of the bubble.

In this section, the simulation of single rising bubble flow is carried out, and the results are compared with past calculation results.

For the first validation, 320 x 480 lattice cells are used and all boundaries are assumed as walls. The parameters are set as $\rho_l = 1$, $\rho_g = 0.001$, $\tau_\varphi = 0.5$, and $W = 5$. Other parameters are determined to fit Eotvos and Morton numbers as in Table 1.

The results of Re and final shapes of bubbles are compared with those of Ryu and Ko [17] in Table 1 and Fig. 8. It is seen that present results are in good agreement with the existing calculation results in quantitative and qualitative terms. For the case C, however, the bubble shapes are somewhat different from each other. The LBM result of Ryu and Ko [17], in particular, seems to be much more stretched sideways than the others. The LB method [13] used in their simulation is hard to apply real densities in two different fluid regions [18]. They mentioned that they used different densities and viscosities for two fluids, but actually used the same values. For high Eo and M, therefore, the rising bubble might be hard to reach to the terminal state because of this characteristic of Ref. [13], and Ryu and Ko were able to get the terminal speed and bubble shape when the bubble reached near the top wall, which has a great effect on making the bubble stretched.

Table 2. Physical parameters and dimensionless numbers for the second rising bubble test.

Case	ρ_l	ρ_g	μ_l/μ_g	Re	Eo
1	1000	100	10	35	10
2	1000	1	100	35	125

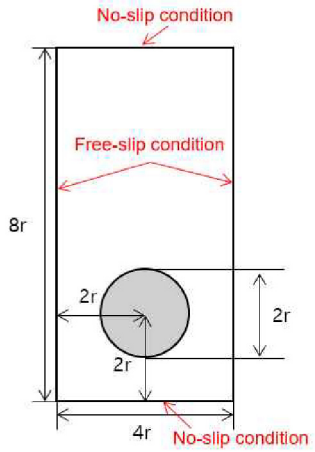

Fig. 9. Initial and boundary conditions for the second rising bubble test.

For the rising bubble problem, Hysing et al. [19] proposed quantitative benchmark configurations and compared several incompressible interfacial flow codes using them. They defined benchmark quantities such as centroid, circularity, and mean rise velocity as follows:

$$\text{Centroid:} \quad \vec{X}_c = \frac{\int_\Omega \vec{x} dx}{\int_\Omega 1 dx} \tag{22}$$

$$\text{Circularity:} \quad \zeta = \frac{P_a}{P_b} = \frac{\pi d_a}{P_b} \tag{23}$$

$$\text{Rise velocity:} \quad \vec{U}_c = \frac{\int_\Omega \vec{u} dx}{\int_\Omega 1 dx} \tag{24}$$

where Ω denotes the bubble region and P_a denotes the perimeter of a circle with diameter d_a, which has an area equal to that of a bubble with perimeter P_b.

For the validation with the above quantities, a second rising bubble test was performed. The initial and boundary conditions can be seen in Fig. 9. The center of the bubble of radius r is located at [2r, 2r] in a [4r x 4r] rectangular domain. The no-slip boundary condition is used at the horizontal top and bottom boundaries, while the free-slip condition is used on the side walls. The physical parameters and dimensionless numbers, which specify the test cases, are listed in Table 2. The Reynolds number and the Eotvos number are defined as

$$Re = \frac{\rho_l U_g L}{\mu_l} \quad \text{and} \quad Eo = \frac{\rho_l U_g^2 L}{\sigma},$$

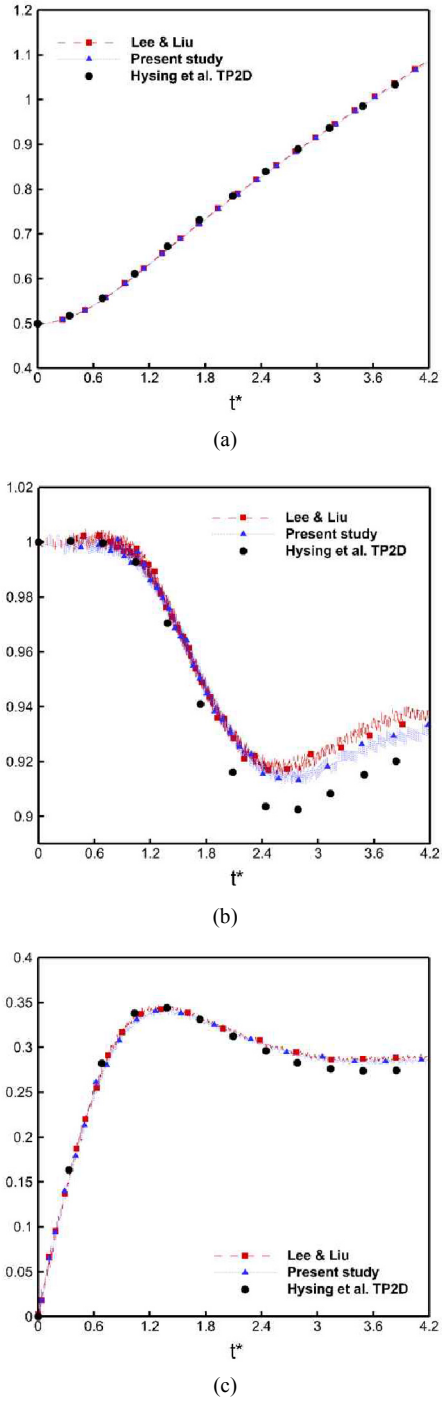

Fig. 10. Test results for the case 1: (a) Centroid; (b) circularity; (c) rise velocity.

where $L = 2r$, and $U_g = \sqrt{2gr}$.

The figures of centroid, circularity, and rise velocity are shown in Fig. 10 which correspond to case 1. The time, t^*, and the rise velocity used in the simulations are non-dimensionalized by the reference time $t = \sqrt{2r/g}$ and U_g, respectively. For comparison, calculation results using Lee & Liu's model are also presented as well as those of Hysing et al. [19]. The plots of centroid and rise velocity agree very well

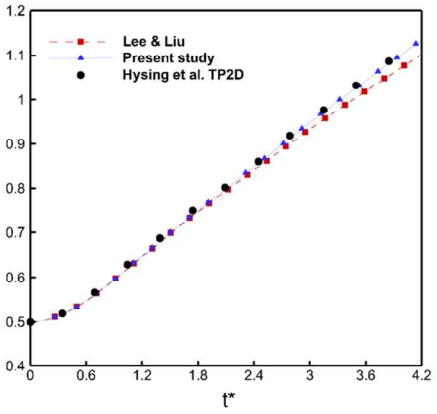

(a)

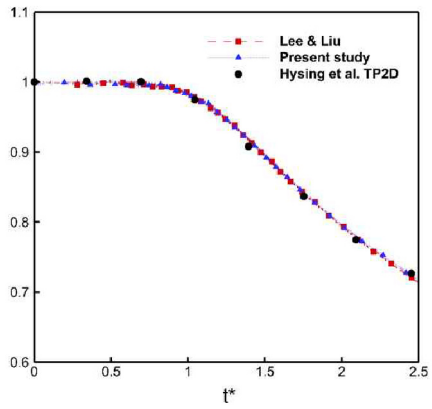

(b)

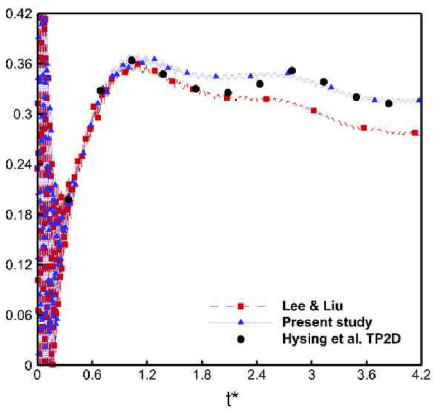

(c)

Fig. 11. Test results for the case 2: (a) Centroid; (b) circularity; (c) rise velocity.

with each other, while the results of LB models slightly deviate from that of Hysing et al. [19] in circularity.

In Fig. 11, the results for the case 2 are presented. In the figure of rise velocity, the bubbles for the LB models appear to vibrate violently in the beginning, which may come from the compressibility effect of the LBM. For large Atwood number, the plots of the three quantities are in good agreement, but the present LB model shows results closer to those of Ref. [19] than Lee & Liu's model.

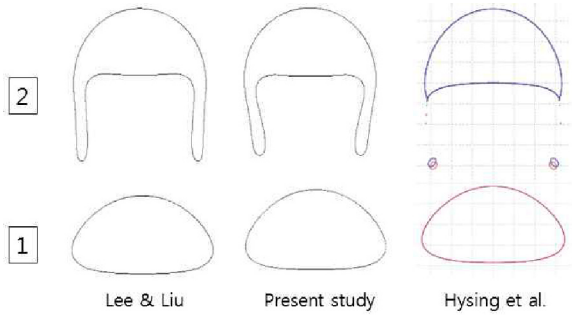

Fig. 12. Comparison of the bubble shape at time $t^* = 4.2$.

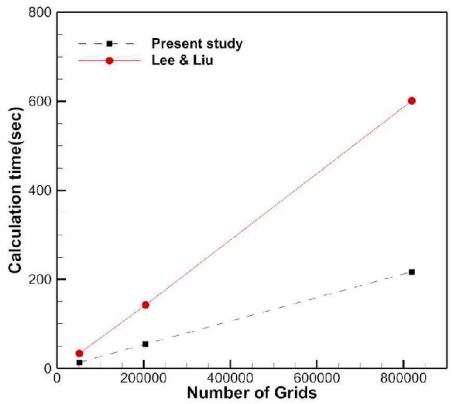

Fig. 13. Comparison of calculation time.

Fig. 12 shows the bubble shape at $t^* = 4.2$. The results of case 1 show that the bubbles are quite similar to each other. For test case 2, three bubbles have a similar shape for the main bulk; however, there is no agreement with respect to the thin filamentary regions. Small satellite droplets can be seen in the result of TP2D [19], while long thin trails still remain in other results like that of MooNMD [19].

For the last test in this section, the calculation time of two LB models was compared. The test case 1 was performed for three different grid sizes of 160x320, 320x640, and 640x1280. The codes for LB models were compiled with the Intel Fortran compiler and the simulations were performed on a computer with Intel Core i7 5820k processor. As seen in Fig. 13, the computation time for both models is growing linearly as the number of grids increases, and Lee & Liu's model takes more than twice as long as present model. Therefore, it is found that current approach has a benefit in computational time.

4. Multiple rising bubbles

Numerical investigations of a rising bubble were mainly focused on a single bubble or two bubbles. When the number of bubbles increases, it is not possible to perform the simulation considering all of them. In such case, a mixture model for the bubbly flow should be applied instead of direct numerical simulation, and it is important to understand the interferences between bubbles to develop a good model.

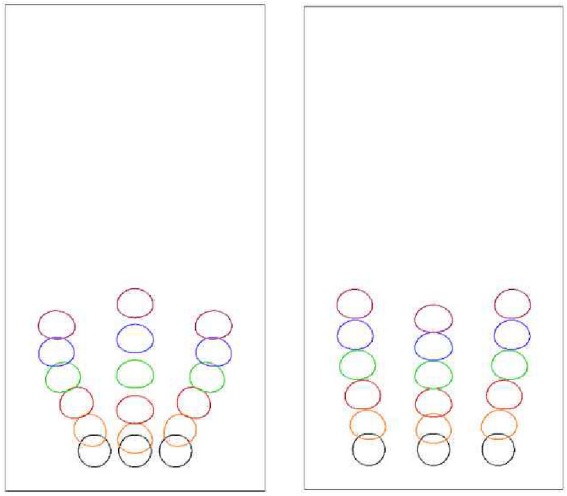

(a) (b)

Fig. 14. Change of the shapes of rising three bubbles for Eo = 5; M = 0.012: (a) Interval 50; (b) interval 80.

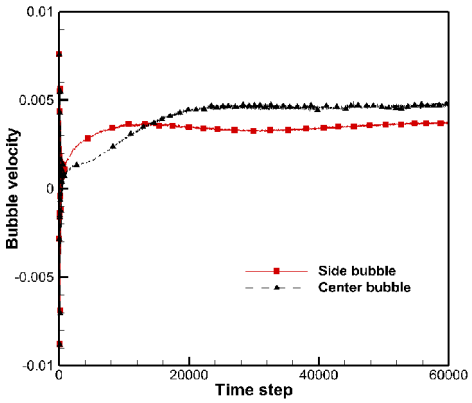

(a)

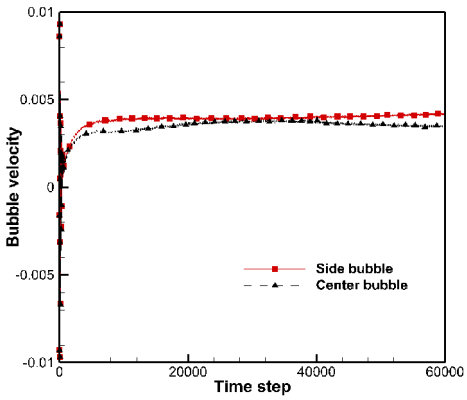

(b)

Fig. 15. Comparison of bubble speeds depending on the location: (a) Interval 50; (b) interval 80.

To observe how the interactions between bubbles occur when three and five bubbles rise at the same time, calculations were performed for the cases that the gap between the center of the bubble was 50 and 80 lattice units. For the computational domain, 320 x 600 and 1000 x 600 lattice cells were used for three and five bubbles, respectively.

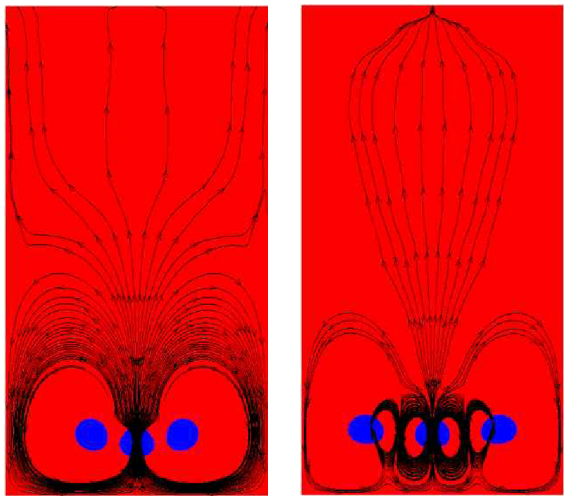

(a) (b)

Fig. 16. Stream traces of the flow near the bubbles: (a) Interval 50; (b) interval 80.

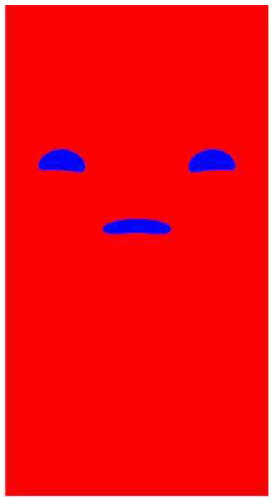

Fig. 17. The shapes of three bubbles for interval 80.

Fig. 14 shows the shapes of the three bubbles changing as they rise when $Eo = 5$, $M = 0.012$. They are presented at every 10000 time steps. In case that the interval between center of bubbles is 50, the rising velocity of the bubble in the center is initially lower than that of the side bubbles, and it is getting greater over time. However, if the bubble interval is 80, the rising velocity of the side bubbles is expected to be higher than the bubble in the middle from the beginning until the end.

The bubble speeds depending on location are compared quantitatively in Fig. 15. For 50 bubble interval, the center bubble rises faster than the side bubbles after 14000 time steps. Fig. 16 shows the stream traces of the flow near the bubbles at the earlier stage. When the bubble interval is 50, rising flow forms strongly in the middle. For the bubble interval 80, however, rising flow from the center is suppressed by the effect of side bubbles, and the bubble in the middle is getting flattened

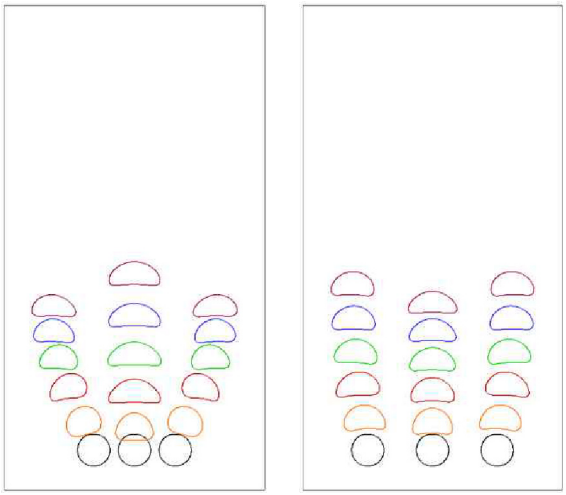

(a) (b)

Fig. 18. Change of the shapes of rising three bubbles for Eo = 16; M = 0.038: (a) Interval 50; (b) interval 80.

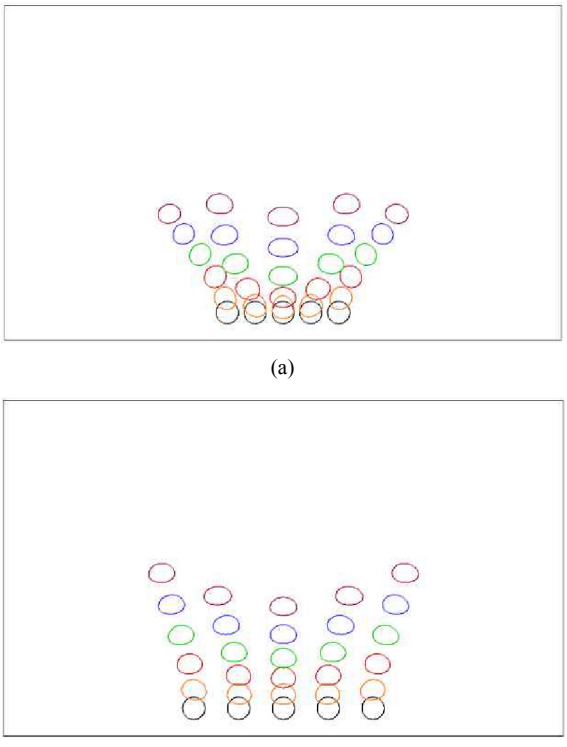

(a) (b)

Fig. 19. Change of the shapes of rising five bubbles for Eo = 5; M = 0.012: (a) Interval 50; (b) interval 80.

by the effect (see Fig. 17). Fig. 18 presents the change of the shape of rising three bubbles at every 6000 time steps when Eo = 16, M = 0.038. The overall trend for bubble rising is similar to that in case of Eo = 5, M = 0.012.

Fig. 19 shows how the shape and position of bubbles change, while the five bubbles rise at the same time for the case of Eo = 5, M = 0.012.

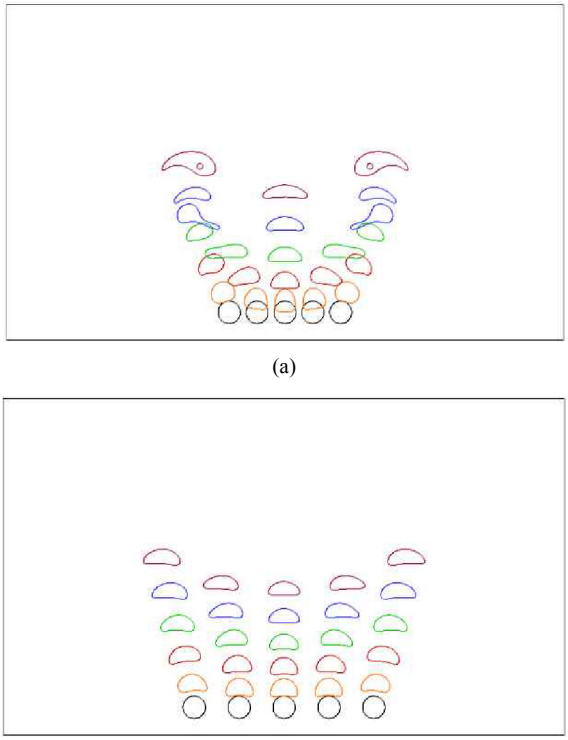

(a) (b)

Fig. 20. Change of the shapes of rising five bubbles for Eo = 16; M = 0.038: (a) Interval 50; (b) interval 80.

When the bubble interval is 80, the bubble rising speed increases as the bubble position gets closer to outside, and that trend is maintained even as time increases. For 50 bubble interval, however, bubble speed in the outermost region is slowing down. In Fig. 20, the shape and position of bubbles are presented at every 6000 time steps for the case of Eo = 16, M = 0.038. The overall trend for bubble rising is similar to that in case of Eo = 5, M = 0.012 for 80 bubble interval. In case of 50 bubble interval, however, it can be seen that two bubbles on the outside are merged into one.

5. Conclusions

In this study a lattice Boltzmann method is proposed for the simulations of multi-phase flow. Using this method, validation tests for the problems of a circular bubble, which is placed at the center of the stationary liquid, Rayleigh-Taylor instability, and single rising bubble were performed. The calculation results, which were compared with those of analytic solution and other numerical studies, show good agreement. When compared with the past LB model, the present method can reduce the calculation time considerably. For the study of multiple rising bubble, some simulations were carried out for three and five bubbles. In the results for three and five bubbles, the difference of interaction of the bubbles was found between the case that bubbles are positioned close to each other and the case that they are not close enough.

Acknowledgments

This work was supported by the National Research Foundation of Korea (NRF) grant funded by the Korea government (MSIP) (No. NRF- 2017R1D1A1B03028324).

Nomenclature

f_α, g_α : Particle distribution function
φ : Order parameter
w_α : Weighting factor
τ_f, τ_φ : Non-dimensional relaxation time
θ_M : Mobility
μ_φ : Chemical potential
σ : Surface tension coefficient

References

[1] Y. Taitel and A. E. Dukler, A model for predicting flow regime transitions in horizontal and near horizontal gas-liquid flow, *AIChE J.*, 22 (1976) 47-55.

[2] J. M. Mandhane, G. A. Gregory and K. Aziz, A flow pattern map for gas-liquid flow in horizontal pipes, *Int. J. Multiphase Flow*, 1 (1974) 537-553.

[3] D. Bhaga and M. E. Weber, Bubbles in viscous liquids: shapes, wakes and velocities, *J. Fluid Mech.*, 105 (1981) 61-85.

[4] J. G. Collier, *Convective Boiling and Condensation,* 2nd Ed., McGraw-Hill, New York (1981).

[5] C. W. Hirt and B. D. Nichols, Volume of fluid (VOF) method for the dynamics of free boundaries, *J. Comput. Phys.,* 39 (1981) 201-225.

[6] J. A. Sethian, *Level Set Methods*, Cambridge University Press, Cambridge, England (1996).

[7] S. O. Unverdi and G. Tryggvason, A front-tracking method for viscous, incompressible, multi-fluid flows, *J. Comput. Phys.*, 100 (1992) 25-37.

[8] A. K. Gunstensen, D. H. Rothman, S. Zaleski and G. Zanetti, Lattice Boltzmann model of immiscible fluids, *Phys. Rev. A*, 43 (1991) 4320-4327.

[9] D. Grunau, S. Chen and K. Eggert, A lattice Boltzmann model for multiphase fluid flows, *Phys. Fluids*, 5 (1993) 2557-2562.

[10] X. Shan and H. Chen, Lattice Boltzmann model for simulating flows with multiple phases and components, *Phys. Rev. E*, 47 (1993) 1815-1819.

[11] M. R. Swift, E. Orlandini, W. R. Osborn and J. M. Yeomans, Lattice Boltzmann simulations of liquid-gas and binary fluid systems, *Phys. Rev. E*, 54 (1996) 5041-5052.

[12] X. He, S. Chen and R. Zhang, A lattice Boltzmann scheme for incompressible multiphase flow and its application in simulation of Rayleigh–Taylor instability, *J. Comput. Phys.*, 152 (1999) 642-663.

[13] H. W. Zheng, C. Shu and Y. T. Chew, A lattice Boltzmann model for multiphase flows with large density ratio, *J. Comput. Phys.*, 218 (2006) 353-371.

[14] T. Lee and L. Liu, Lattice Boltzmann simulations of micron-scale drop impact on dry surfaces, *J. Comput. Phys.*, 229 (2010) 8045-8063.

[15] J. J. Huang, C. Shu and Y. T. Chew, Mobility-dependent bifurcations in capillarity-driven two-phase fluid systems by using a lattice Boltzmann phase-field model, *Int. J. Numer. Methods Fluids*, 60 (2009) 203-225.

[16] A. J. Briant and J. M. Yeomans, Lattice Boltzmann simulations of contact line motion. II. Binary fluids, *Phys. Rev. E,* 69 (2004) 031603.

[17] S. Ryu and S. Ko, A comparative study of lattice Boltzmann and volume of fluid method for two-dimensional multiphase flows, *Nucl. Eng. Technol.*, 44 (6) (2012) 623-638.

[18] N. Jeong, A comparative study of free energy based lattice Boltzmann models for two-phase flow, *J. Comput. Fluids Eng.*, 24 (2) (2019) 69-75.

[19] S. Hysing, S. Turek, D. Kuzmin, N. Parolini, E. Burman, S. Ganesan and L. Tobiska, Quantitative benchmark computations of two-dimensional bubble dynamics, *Int. J. Numer. Meth. Fluids*, 60 (2019) 1259-1288.

Namgyun Jeong received his B.S., M.S. and Ph.D. from the Division of Mechanical Engineering of KAIST in 1999, 2001 and 2007, respectively. His research is focused on computational fluid dynamics. The subjects of his interest are multiphase flow and rarefied gas flow.